



# Deep through-flow in the Bight Fracture Zone and its imprint in the Irminger Sea

Tillys Petit<sup>1,2</sup>, Virginie Thierry<sup>1</sup>, and Herlé Mercier<sup>1</sup>

<sup>1</sup> Univ Brest, CNRS, Ifremer, IRD, Laboratoire d'Océanographie Physique et Spatiale (LOPS), IUEM, F29280, Plouzané, France

<sup>2</sup> Present address: National Centre for Atmospheric Science, Department of Meteorology, University of Reading, Reading, UK

Correspondence to: Tillys Petit (t.petit@reading.ac.uk)

**Abstract.** Iceland-Scotland Overflow Water (ISOW) is exported from the Nordic Seas into the Iceland Basin to feed the lower limb of the Meridional Overturning Circulation. The Bight Fracture Zone (BFZ) is known to be a major route for ISOW toward the Irminger Sea, but the role of this gateway in the evolution of ISOW properties over the subpolar gyre is unclear. A combination of ship-based and Deep-Argo data gathered between 2015 and 2018 allows us to investigate the pathways and hydrological evolution of ISOW as it flows through the BFZ, as well as its influence on the ISOW properties in the Irminger Sea. The ISOW flow through the BFZ amounts to  $0.76 \pm 0.2$  Sv and is mainly fed by the lighter part of the ISOW layer flowing west of  $29\text{-}30^\circ\text{W}$  as part of the East Reykjanes Ridge Current in the Iceland Basin. In the rift valley of the BFZ, between an eastern and a western sill, the bathymetry of the BFZ shapes a cyclonic circulation along which the ISOW layer is homogenised. The largest changes in ISOW properties are however observed downstream of the western sill, at the exit of the BFZ. There, ISOW is mixed isopycnally with comparatively fresher ISOW from the Irminger Sea and lies over denser ISOW that entered the Irminger Sea south of the BFZ. These fresher ISOW result from the erosion of the ISOW core by mixing with inflows from the interior of the Irminger Sea as ISOW flows northward from the Charlie-Gibbs Fracture Zone. Hence, our analysis reveals the key role of the BFZ through-flow in compensating these inputs of fresh inflows along the northward Irminger Current.

## 1 Introduction

Iceland-Scotland Overflow Water (ISOW) is a major component of the lower limb of the Meridional Overturning Circulation (MOC). Formed by mixing between overflows from the Nordic Seas, Atlantic Water and Labrador Sea Water (LSW), ISOW is characterized by potential density higher than  $27.8 \text{ kg m}^{-3}$  and salinity higher than 34.94 downstream of the Iceland-Scotland-Faroe Ridge (Hansen & Østerhus, 2000; Johns et al., 2021; Saunders, 1994). ISOW is then carried southwestward along the Icelandic shelf (Kanzow & Zenk, 2014) and subsequently along the eastern flank of the Reykjanes Ridge within several veins of the East Reykjanes Ridge Current (Koman et al., 2020; Xu et al., 2010). While the Charlie-Gibbs Fracture Zone is known as the main ISOW gateway toward the Irminger Sea (Saunders, 1994), Xu et al. (2010) identified the Bight Fracture Zone



(BFZ), a deep and wide gap of the Reykjanes Ridge near 57°N, as a second major route for ISOW toward the Irminger Sea. The importance of the BFZ for the connection of deep water between the two basins is supported by float trajectories (Bower et al., 2002; Kanzow & Zenk, 2014; Lozier et al., 2022) and the OVIDE data analysis (Daniault et al., 2016). More recently, 35 Petit et al. (2019) estimated that one third of these southward veins reaches the Irminger Sea through the BFZ, the remainder crossing the ridge through deeper fractures further south.

At about 58.8°N, Daniault et al. (2016) highlighted a strong asymmetry of the ISOW properties between the eastern and western flanks of the Reykjanes Ridge. Petit et al. (2019) showed that the asymmetry of the ISOW properties persists north and south of the BFZ, at about 56.4°N and 63°N. The evolution of the ISOW properties from the Iceland Basin to the Irminger 40 Sea is attributed to mixing through the complex bathymetry of the ridge. Analyzing microstructure and CTD data from the OVIDE line, Ferron et al. (2016) showed that dissipation rates (vertical mixing) was enhanced over the flanks of the Reykjanes Ridge. Similarly, fracture zones are known sites of large modification of water mass properties (Mercier et al., 1994). Recent studies based on moorings (Bower & Furey, 2017) and Deep-Argo floats (Racapé et al., 2019) deployed in the Charlie-Gibbs Fracture Zone (CGFZ) have pointed out the mixing between ISOW and surrounding water masses, including North-East 45 Atlantic Deep Water, Lower Deep Water and LSW.

Understanding the propagation and evolution of ISOW is crucial to characterize the evolution of the lower limb of the MOC over the North-Atlantic Subpolar Gyre and the propagation of climate signals to the rest of the ocean. While the role of the CGFZ in the spreading pathways of ISOW has been investigated for decades (Bower & Furey, 2017; Racapé et al., 2019; Saunders, 1994; Xu et al., 2010; Zou et al., 2017, 2020), the lack of direct observations prevented us to investigate the role of 50 the BFZ.

In this study, we provide new insights on the ISOW flow through the BFZ in combining data from high-resolution hydrographic sections and Deep-Argo floats acquired at key locations in the BFZ. The article is organized as follows. Section 2 presents the data and methods used for the study. The ISOW pathways, transport and property evolution through the BFZ are analyzed in Section 3. The imprint of the BFZ through-flow on the evolution of ISOW in the Irminger Sea is also discussed in Section 3. 55 Section 4 summarizes the results and discusses their implications for the lower limb of the MOC.

## 2 Data and Methods

### 2.1 Bathymetry of the Bight Fracture Zone

The deepening of the Reykjanes Ridge southward from Iceland is associated with several fracture zones, including the BFZ at 57°N (Figure 1). The BFZ axis extends quasi-zonally from the Iceland Basin to the Irminger Sea and intersects the rift valley 60 of the Reykjanes Ridge at 56.75°N/34.17°W. The BFZ entrance is composed of a narrow sill (8.7-km wide – following the 2000-m isobaths) at 56.73°N/33.72°W along the eastern side of the rift valley. It reaches a bottom depth of ~2150 m and is referred herein as the Eastern Sill (Figure 1c).



Immediately west of the Eastern Sill, the axis of the BFZ intersects the rift valley of the Reykjanes Ridge that is oriented northeast – southwest and reaches bottom depths larger than 2500 m (Figure 1c). A second sill, referred to as the Western Sill, is located on the western side of the rift valley (56.75°N/35.55°W). It reaches a bottom depth close to that observed for the Eastern Sill, although it is larger when considering the 2000-m isobaths (11.3 km). At the approach of the Irminger Sea, the Western Sill connects to two **basins** deeper than 2500 m and separated by a seamount with a summit that lies at about 1700 m.

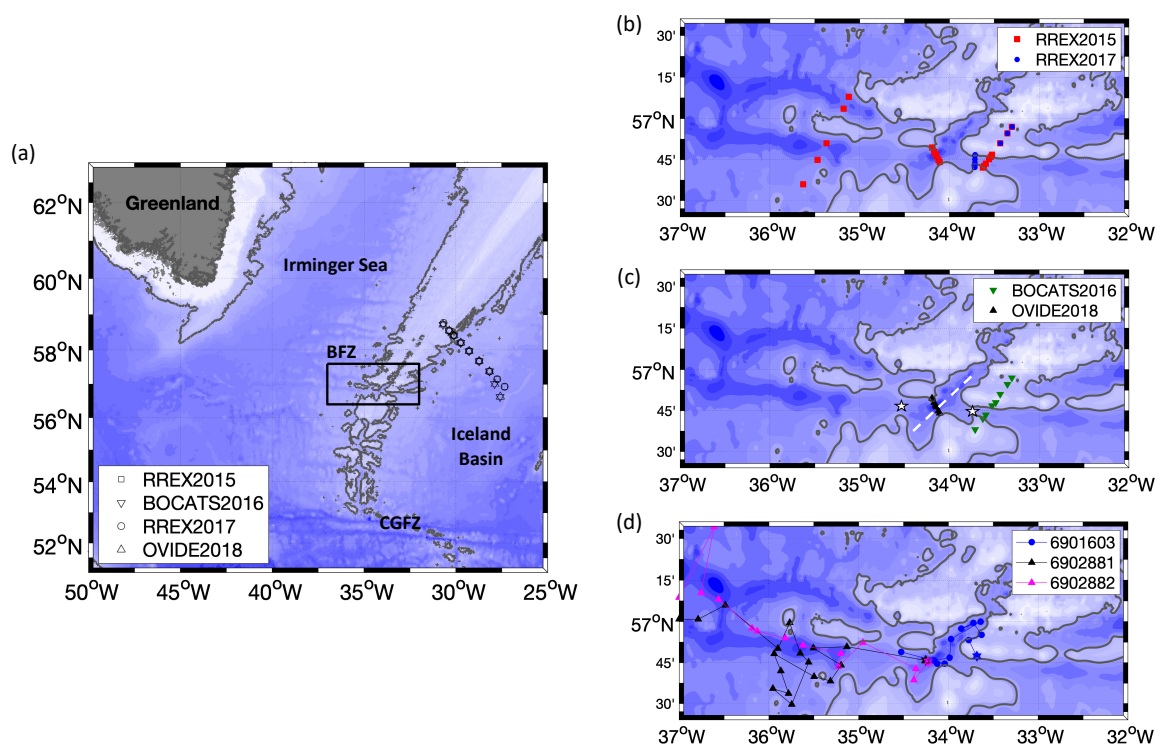


**Figure 1.** Bathymetry of the Reykjanes Ridge from ETOPO1 with 200-m isobaths spacing for (a) the eastern subpolar gyre and (b,c,d) the region of the Bight Fracture Zone as identified by the black rectangle in panel (a). The grey line outlines the 2100-m isobaths. ~~The deepest bathymetries are represented with darkest blue.~~ (a) Hydrographic stations realized along the OVIDE line during the RREX15, BOCATS16, RREX17 and OVIDE18 cruises. (b) Hydrographic stations realized in the BFZ during the RREX15 and RREX17 cruises (c) Hydrographic stations realized in the BFZ during the BOCATS16 and OVIDE18 cruises. The axis of the rift valley of the Reykjanes Ridge crosses the Middle section and is identified by a white dashed line. The Eastern and Western sills are identified by white stars. (d) Positions of the Deep-Array float profiles for #6902881 (cycles 1-14), #6902882 (cycles 1-18) and #6901603. All floats show overall westward trajectories from their deployment position identified by a star.

## 2.2 Hydrographic and velocity sections

This study is based on high-resolution measurements obtained during four cruises between 2015 and 2018 at key locations of the BFZ (Figure 1 and Table 1). Two sections are localized within the BFZ. The East section was occupied at the eastern entrance of the BFZ in 2015, 2016 and 2017. Depending on the cruises, it was located either **at** or 5.5 km upstream of the Eastern Sill. The Middle section was occupied in the rift valley in 2015 and 2018. At the exit of the BFZ, the West section



intersected the two **basins** west of the Western Sill in 2015. These three hydrographic sections were designed to study the deep circulation and associated evolution of ISOW that enters the BFZ from the Iceland Basin, circulates in the rift valley of the Reykjanes Ridge, and exits the BFZ toward the Irminger Sea.

85 Twenty-one CTDO<sub>2</sub> (Conductivity Temperature Depth Oxygen) stations were first carried out along the three sections (stations 16 – 20 and 96 – 107) in June 2015 on the French N/O Thalassa during the RREX15 cruise (Branellec & Thierry, 2016). It consists of six stations at the East section, six stations at the Middle section and four stations at the West section. The nominal station spacing was less than 2 km along the East and Middle sections and less than 10 km along the West section. We also use station 122 carried out at 35.1°W/52.7°N during the RREX15 cruise for a comparison with the hydrological properties in  
90 the CGFZ.

A year later, the BOCATS16 cruise carried out five CTDO<sub>2</sub> stations along the East section in July 2016 on the Spanish B/O Sarmiento de Gamboa (stations 105-109; Branellec & Lherminier, 2017).

In addition to these two cruises, the RREX17 cruise carried out six CTDO<sub>2</sub> stations at the East section in August 2017 on the French N/O l'Atalante (stations 86 – 91; Branellec & Thierry, 2018). The stations were 5.5 km west of those carried out during  
95 RREX15 and BOCATS16 to intersect the Eastern Sill of the BFZ. For simplicity, we refer to this section as the East section as well.

Finally, the OVIDE18 cruise carried out six CTDO<sub>2</sub> stations along the Middle section in July 2018 on the French N/O Thalassa (stations 103 – 108; Branellec et al., 2019).

During the four cruises, CTDO<sub>2</sub> stations were also carried out along the so-called OVIDE line (Figure 1a) that intersects the  
100 Reykjanes Ridge at 31.3°W/58.8°N (Lherminier et al., 2007). Here, we consider the stations on the eastern side of the Reykjanes Ridge, from 27.2°W to 30.7°W, to analyze the along-stream evolution of ISOW upstream of the BFZ.

The accuracies of the CTDO<sub>2</sub> measurements are better than 0.002°C, **0.002** 1 dbar and 1.5 μmol kg<sup>-1</sup> for the four cruises, except for the dissolved oxygen concentration for which the accuracy was estimated at 2 μmol kg<sup>-1</sup> for OVIDE18. Figures A1 and A2 show the salinity and potential temperature of the East and Middle sections.

105 The CTD rosette was equipped with a 300 kHz downward and a 150 kHz upward looking L-ADCP (Lowered Acoustic Doppler Current Profiler, RD Instruments). The upper layer current velocity components were measured by two S-ADCPs (Shipboard Acoustic Doppler Current Profiler, RD Instruments) operating at 38 kHz (OS38) and 150 kHz (OS150), with the exception of BOCATS16 for which S-ADCPs operated with a combination of 75 kHz (OS75) and 150 kHz (OS150). The calibrations and processing of these measurements were identical for all four cruises, as described by (Petit et al., 2018).

110 Geostrophic velocities and the associated gridded transports (Figure 2 and Table 3) were estimated from these ADCP and hydrological measurements following Petit et al. (2018). The geostrophic velocities are evaluated by comparison to the L-ADCP velocities at the East and Middle sections (Figures A3 and A4). Note that L-ADCP measurements provide local



115 velocities at each hydrographic station while geostrophic velocities are averaged velocities between two successive stations (Lherminier et al., 2007), so we cannot expect a perfect agreement between the two data sets. Nevertheless, the comparison of the amplitude and spatial structure of the velocity field reveals the remarkable agreement between the geostrophic and L-ADCP velocities for each section. The largest difference in velocity is found at the Eastern Sill in 2017 where the geostrophy-based velocity in the ISOW core is about  $-0.36 \text{ m s}^{-1}$ , while the L-ADCP-estimated velocity is about  $-0.14 \text{ m s}^{-1}$ .

120 **Table 1.** Summary of the sections occupied during the four hydrographic cruises and the associated station numbers. Details on the cruises and on the locations of the stations can be found in Branellec & Thierry (2016), Branellec & Lherminier (2017), Branellec & Thierry (2018) and Branellec et al. (2019).

Cruise	Date	Ship	Sections	Stations
RREX15	June 2015	N/O Thalassa	West section East section Middle section	16 – 20 96 – 101 102 – 107
Bocats16	July 2016	B/O Sarmiento de Gamboa	East section	105 – 109
RREX17	August 2017	N/O l’Atalante	East section	86 – 91
OVIDE18	July 2018	N/O Thalassa	Middle section	103 – 108

### 2.3 Deep-Arvor floats

125 Data from three Deep-Arvor floats are used to assess the pathway and hydrological evolution of ISOW as it flows westward through the BFZ. The Deep-Arvor floats are Argo floats profiling down to 4000 m (Le Reste et al., 2016; Le Traon et al., 2020) and returning every 10 days top-to-bottom profiles of temperature, salinity and dissolved oxygen concentration as a function of pressure. One Deep-Arvor float (WMO#6901603) was deployed at the East section during RREX17 (station 89 at  $56.73^{\circ}\text{N}/33.72^{\circ}\text{W}$ ) and two Deep-Arvor floats (WMO#6902881, #6902882) were deployed simultaneously at the Middle section during OVIDE18 ( $56.80^{\circ}\text{N}/34.17^{\circ}\text{W}$ ) (Table 2). The Deep-Arvor float #6901603 completed 12 cycles before it died on 26 November 2017. Floats #6902881 and #6902882 completed a few cycles in the BFZ before exiting the fracture zone and drifting in the Irminger Sea. The three floats drifted mostly in the range 1900-2100 dbar within the ISOW core layer. 130 #6901603 grounded at cycles 2, 11 and 12 and drifted at shallower pressure during these cycles. Trajectories within the ISOW layer of the Deep-Arvor floats are considered from cycle 2 because the floats are programmed to rise to the surface immediately after reaching their parking depth at the end of the first descent.



Temperature, conductivity and pressure were measured using a Seabird SBE41CP CTD sensor with a target accuracy of 0.002 °C, 0.004 and 7 dbar, respectively. The salinity data were corrected following the procedure specified for Deep-Argo floats (Cabanes et al., 2016; Wong et al., 2021). A compressibility term (CPcor) was applied to correct a pressure dependent conductivity sensor bias. For the three floats, the nominal CPcor value provided by Seabird ( $CPcor = -9.57e-08 \text{ dbar}^{-1}$ ) is replaced by the Argo recommended value,  $CPcor = -13.5e-08 \text{ dbar}^{-1}$ . No further salinity bias or drift was detected for #6901603 and #6902882, while #6902881 was corrected for a salty bias of 0.002.

140 **Table 2.** Details on the deployment and parking depth of the three Deep-Arvor floats.

Float WMO	6901603	6902881	6902882
Date of deployment	6 August 2017	8 July 2018	8 July 2018
Cruise	RREX2017	OVIDE2018	OVIDE2018
Number of cycles	12	>86 cycles (active)	>86 cycles (active)
Parking depths	Cycle 2: 1200dbar Cycle 3 – 10: 2100dbar Cycle 11: 1100dbar Cycle 12: 1500dbar	Cycle 2 – end: 1900 - 2100dbar	Cycle 2 – end: 1900 - 2100dbar

### 3 Results

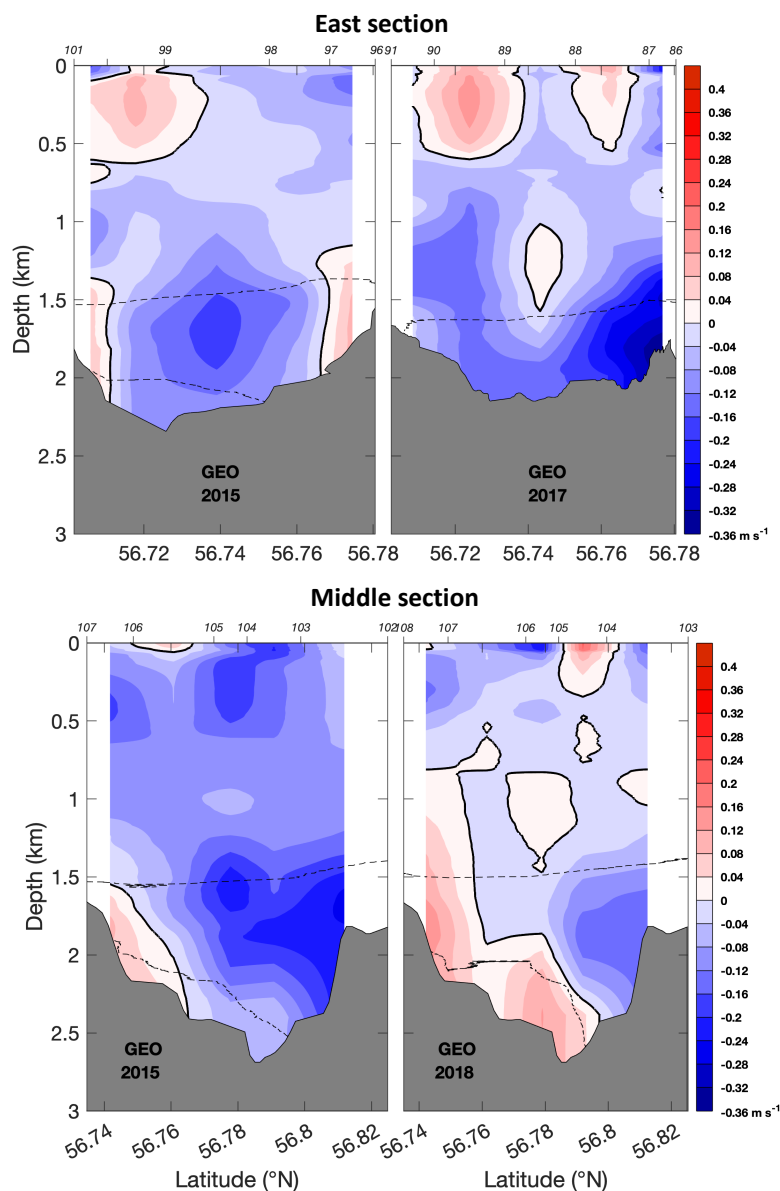
In this section, we use the Deep-Arvor floats and the hydrographic sections of the four surveys to describe the propagation and hydrological evolution of ISOW as it flows through the BFZ from the East Reykjanes Ridge Current to the Irminger Sea.

#### 145 3.1 Propagation of ISOW through the BFZ

The potential temperature-salinity ( $\theta$ - $S$ ) properties of ISOW at the BFZ are compared to those observed in the East Reykjanes Ridge Current along the OVIDE section (Figure 3). The comparison in the density range  $27.8\text{--}27.87 \text{ kg m}^{-3}$  reveals three geographical area along the section ISOW east of  $29^\circ\text{W}$  is fresher than that observed in the BFZ, while ISOW west of  $30^\circ\text{W}$  has  $\theta$ - $S$  properties close to those observed in the BFZ. The  $\theta$ - $S$  properties between  $29\text{--}30^\circ\text{W}$  are variable in time, being fresher than at the BFZ in 2015 and 2016 but matching the ISOW properties in the BFZ in 2017 and 2018. This shows that the BFZ



is mainly fed by ISOW flowing along the eastern flank of the Reykjanes Ridge west of 29–30°W. Nevertheless, ISOW at the **entrance** of the BFZ is lighter than  $27.87 \text{ kg m}^{-3}$  while ISOW observed west of 29–30°W reaches denser values. Then, only the lightest variety of ISOW localized west of 29–30°W along the OVIDE section enters the BFZ.



155 **Figure 2.** Geostrophic velocity sections ( $\text{m s}^{-1}$ ) along the **(upper panels) East section** in 2015 and 2017 and **(lower panels) Middle section** in 2015 and 2018. Positive values correspond to eastward velocities. The black bold line outlines the 0 isotach. The dashed black lines indicate the potential density  $\sigma_0 = 27.8$  and  $27.85 \text{ kg m}^{-3}$ . Bathymetry acquired from the echo-sounder of the ship survey is added in grey. Locations of the hydrographic stations are indicated on the top axis.



160 Once at the Eastern Sill of the BFZ, the following analysis relies on a comparison of the velocity fields and hydrological properties observed in the ISOW layer between the East and Middle sections, and along the pathway of the Deep-Arvor float #6901603. The geostrophic velocity section acquired in 2016 is not discussed here because the sampling of the stations was not appropriate to capture the ISOW transport at depths higher than ~1500 m at the Eastern Sill.

A comparison of the velocity fields observed in 2015 and 2017 in the ISOW layer of the East section reveals differences in the amplitude and location of the ISOW through-flow (Figure 2). In 2015, a westward flow is intensified at the center of the sill (56.74°N), while a weak eastward flow is observed along its northern wall (56.77°N). In 2017, a westward flow is observed all along the section and is intensified along the northern wall of the sill. These differences can be due to interannual variability of the inflow from the Iceland Basin, or to differences in bottom friction within the narrow channel of the BFZ entrance, as the East section in 2015 is localized slightly upstream in the channel compared to the East section in 2017 (Figure 1b). The ISOW transport is estimated at  $-0.66 \pm 0.1$  Sv in 2015 and  $-0.54 \pm 0.2$  Sv in 2017, which represents 55.5 % and 48.6 % of the top-to-bottom transport, respectively (Table 3).

At the Middle section, the velocity field in the ISOW layer is composed of a westward flow along the northern wall of the rift valley and an eastward flow along its southern wall in 2015 and 2018 (Figure 3). This circulation at the Middle section suggests a cyclonic pathway for ISOW in the rift valley of the Reykjanes Ridge. The associated top-to-bottom and ISOW transports are five times weaker in 2018 than in 2015 (Table 3), although the ISOW transport represents the same proportion of the top-to-bottom transport for these two years (42.7 % in 2015 and 44.1 % in 2018). The reduced ISOW transport in 2018 is due to an overall reduced westward flow combined with an enhanced eastward flow, which is composed of an additional core of ISOW at 56.78°N that is not observed in 2015.

**Table 3.** Geostrophic top-to-bottom and ISOW transports (Sv) across the East and Middle sections. ISOW is defined by  $\sigma_0 > 27.8 \text{ kg m}^{-3}$  and salinity higher than 34.94. Errors are estimated following Petit et al. (2018).

Section	East S. 2015	East S. 2017	Middle S. 2015	Middle S. 2018
Top-to-bottom transports (Sv)	$-1.19 \pm 0.2$	$-1.11 \pm 0.2$	$-2.93 \pm 0.2$	$-0.59 \pm 0.1$
ISOW transports (Sv)	$-0.66 \pm 0.1$	$-0.54 \pm 0.2$	$-1.25 \pm 0.1$	$-0.26 \pm 0.1$

180

The hypothesis of a cyclonic pathway for ISOW in the rift valley is supported by the trajectory of the Deep-Arvor #6901603 float in summer 2017 (Figure 1c). The float drifted northward at 1200 dbar during its first two cycles from the Eastern Sill of the BFZ (Table 2). Although this parking depth is not associated with ISOW density, we note that its pathway is parallel to the 2100-m isobath of the seamount north of the Eastern Sill. North of the seamount, the float drifted within the ISOW layer at





185 2100 dbar and reached the northern part of the rift valley at cycle 5. Finally, the float drifted mainly south-westward, and then westward as it crossed the western sill of the BFZ at its last cycle. Hence, the trajectory of the #6901603 Deep-Arvor float sketches a cyclonic pathway in the rift valley of the Reykjanes Ridge during its 12 cycles.

The transformation of ISOW in the BFZ is now analyzed by comparing the  $\theta$ -S properties of ISOW between the East and Middle sections in 2015 (Figure 4 a-b). The  $\theta$ -S range of variation on a given isopycnal does not exceed  $0.01^\circ\text{C}$  and **0.005** between the East and Middle sections. This **show** that ISOW does not exhibit a significant evolution of its hydrological properties by isopycnal mixing between the Eastern and Western sills of the BFZ in 2015. This is also true when considering the Deep-Arvor float properties (not shown). A decrease of  $\sim 0.015 \text{ kg m}^{-3}$  in density of the near bottom water is however observed at the Middle section. This can possibly be ascribed to the bathymetry of the Eastern Sill in case the densest water cannot overflow the topographic obstacle of the sill at 2150-m depth localized between the two sections (black star in Figure 195 4b). This is however not supported by the velocity section at the East section in 2015 (Figure 2) **that** shows westward velocities down to the bottom, so that we rather interpret this property change as evidence of vertical mixing.

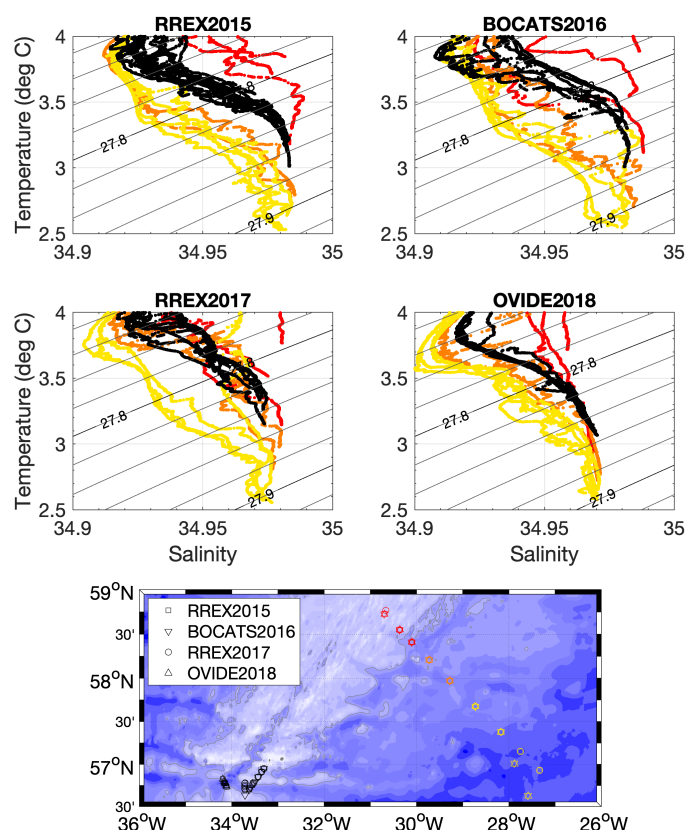
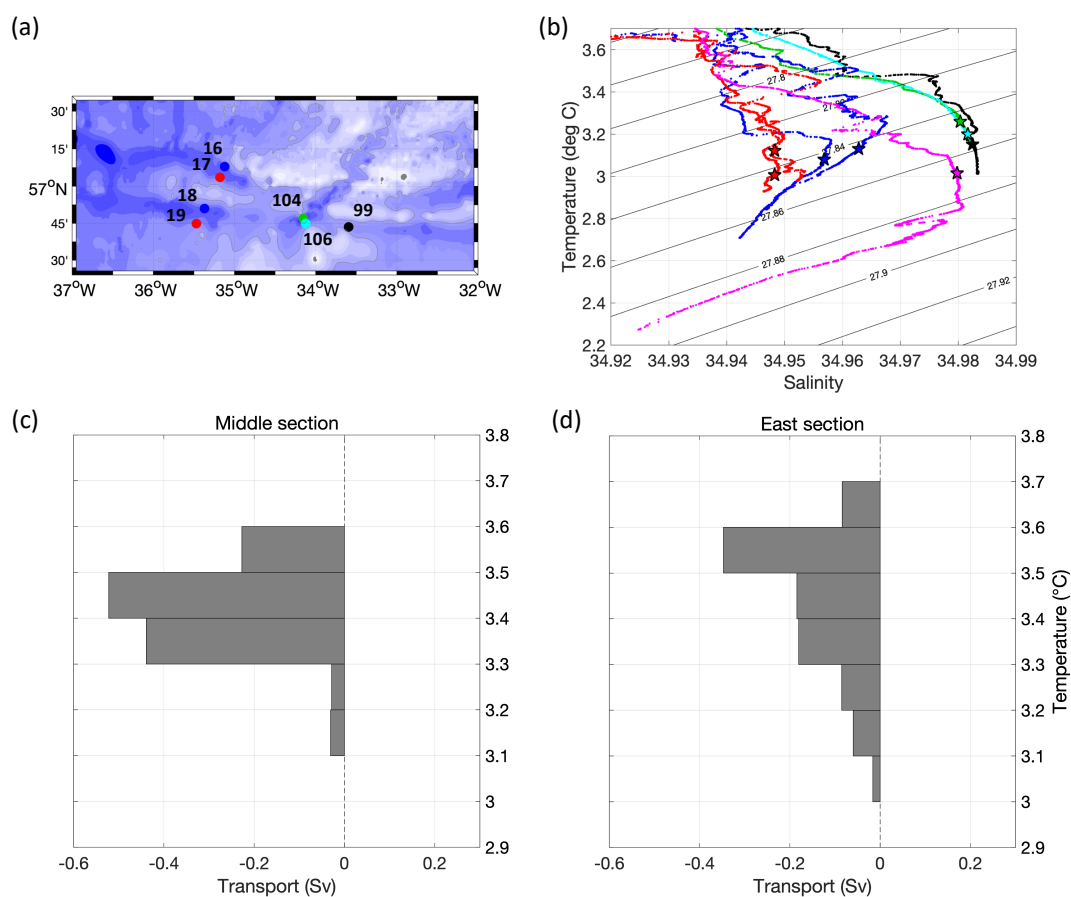


**Figure 3.**  $\theta$ -S diagram of the (color) southward along-ridge flow and (black) westward cross-ridge flow through the BFZ for each cruise indicated in the lower panel.



200 To better show this vertical mixing, we now consider the distribution of ISOW transport in temperature bins of  $0.1^{\circ}\text{C}$  at these two sections (Figure 4 c-d). Their comparison reveals a net decrease in ISOW transport in the temperature bins  $3.7^{\circ}\text{C}$  and  $3.2^{\circ}\text{C}$  from the East to the Middle section. On the contrary, the ISOW transport significantly increases in the intermediate temperature bins  $3.3\text{--}3.5^{\circ}\text{C}$  at the Middle section. The temperature range of the ISOW layer is thus reduced by  $0.3^{\circ}\text{C}$  during its transit through the BFZ, with 77% of ISOW localized within the  $3.3\text{--}3.6^{\circ}\text{C}$  bins at the Middle section. These results  
 205 highlight that ISOW is mainly homogenized as it flows westward in the BFZ, likely due to a vertical mixing within the ISOW layer.



210 **Figure 4.** (a, b)  $\theta$ -S diagram of ISOW localized at the entrance of the BFZ (station 99 at the East section), in the rift valley (stations 104 and 106 at the Middle section) and at the exit of the BFZ (West section) for RREX15. At the West section, the northern stations of each basin are in blue (stations 16 and 18) and the southern stations are in red (stations 17 and 19). Purple dots indicate the  $\theta$ -S properties of station 122 for RREX2015, which is localized in the westward core of ISOW in the CGFZ, at  $35.1^{\circ}\text{W}/52.7^{\circ}\text{N}$  (Petit et al., 2018). Each station is localized in the ISOW core of the sections. Stars indicate the 2150-m isobath for each profile, e.g. the bottom depth of the Eastern Sill. (c, d) Transports (Sv) cumulated in temperature bins of  $0.1^{\circ}\text{C}$  and averaged at the (d) East and (c) Middle sections in 2015.



### 215 3.2 Imprint of the BFZ through-flow in the Irminger Sea

To assess the evolution of ISOW as the overflow exits the BFZ through the two western basins, we use L-ADCP profiles at the West section in 2015 and two Deep-Arvor floats deployed at the Middle section in 2018, #6902881 and #6902882. The analysis is based on L-ADCP instead of geostrophic velocities because the distance between the stations at the West section is too large to resolve the ISOW flow in these narrow basins.

220 The data suggests that the main exit pathway for ISOW follows the northern walls of the western basins and that incursion of dense water from the Irminger Sea follows the southern walls, leading to a mixing between ISOW from the Irminger Sea and ISOW from the BFZ. Indeed, the RREX15 ship-based data show that each of the western **basins** is composed of a westward flow along the northern walls (stations 16 and 18) and an eastward flow along the southern walls (stations 17 and 19) in the ISOW layer (Figure 5). Accordingly, the two Deep Arvor floats followed the northern wall of the southernmost basin when  
 225 exiting the BFZ until at least 35.5°W (Figure 1d). The trajectory of float #6902881 became more chaotic further west.

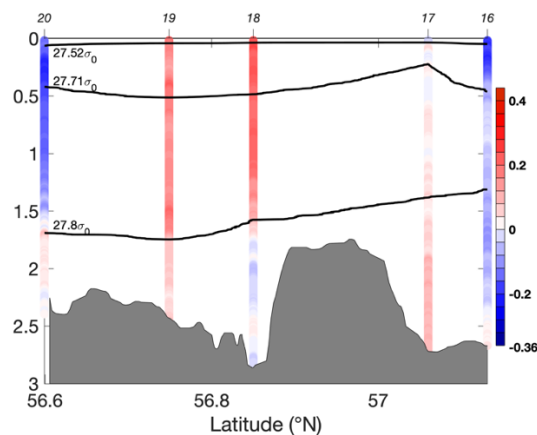


**Figure 5.** Velocity profiles ( $\text{m s}^{-1}$ ) from L-ADCP measurements along the West section in 2015. Positive values correspond to eastward velocities. The dashed black lines indicate the potential density  $\sigma_0 = 27.52, 27.71$  and  $27.8 \text{ kg m}^{-3}$ . Bathymetry acquired from the echosounder of the ship survey is added in grey. Locations of the hydrographic stations are indicated on the top axis.

230 Both the Deep-Arvor floats and the RREX15 ship-based data reveal that ISOW is colder and fresher in the western **basins** than in the rift valley (Figures 4b and 6 c-d). The RREX15 data additionally show that, for density lighter than  $\sigma_0 < 27.855 \text{ kg m}^{-3}$ , the  $\theta$ -S properties found along the northern walls of the **basins** are at intermediate positions between those in the BFZ and those observed along the southern walls of the basins. This suggests that ISOW exiting the BFZ along the northern walls is formed by isopycnal mixing between the BFZ through-flow and colder and fresher ISOW **from the Irminger Sea**. In the lower  
 235 part of the layer ( $\sigma_0 > 27.855 \text{ kg m}^{-3}$ ), ISOW along the northern walls is fresher than in its upper layer. This lower part of the **layer cannot be renewed by BFZ through-flow whose density is lower than  $27.855 \text{ kg m}^{-3}$ , and must originate from the Irminger Sea and through-flows south of the BFZ. The ISOW layer is thus a superposition of ISOW of different origins: its upper part**



is mainly composed of BFZ through-flow that mixes with fresher and colder ISOW entering the western **basins** from the Irminger Sea, while its lower part is mainly composed of denser ISOW **flowing from the Irminger Sea**. Interestingly, the  
240 superposition of these two ISOW layers creates a maximum in salinity at  $27.83 \text{ kg m}^{-3}$  (Figures 4b and 6d), which was not observed at the Eastern and Western sills.

The Deep-Arvor floats then spread in the Irminger Sea and mix with surrounding water masses along their pathways. The two floats followed similar pathways **at a few week interval** heading toward the tip of Greenland and being abruptly diverted northeastward to join the Irminger Current (Figure 6 a-b). However, upon reaching  $\sim 39^\circ\text{W}$  at the exit of the BFZ, the float  
245 #6902882 first headed southward along the Reykjanes Ridge until  $54^\circ\text{N}$  and then turned back northward until  $58^\circ\text{N}$ . The southward spreading of this float along the western flank of the Reykjanes Ridge provides an opportunity to investigate the influence of the BFZ through-flow on the ISOW properties flowing northward from deeper fracture zones south of the BFZ. More precisely, we now compare the  $\theta$ -S properties of ISOW at the western exit of the BFZ and in the vicinity of the CGFZ.

The RREX15 ship-based data shows that the westward core of ISOW at CGFZ reaches a maximum in salinity at  $27.88 \text{ kg m}^{-3}$  while the maximum in salinity observed in the western **basins** of the BFZ is at  $27.83 \text{ kg m}^{-3}$  (Figure 4b). The difference in  
250 density for the ISOW core between the two fracture zones is confirmed by the along-track properties of the float #6902882 (Figure 6 d-e). The core of ISOW is then eroded toward lower densities as the float leaves the vicinity of the CGFZ to reach BFZ latitudes (Figure 6 e-f). The maximum in salinity is now observed at lower densities ( $27.81 \text{ kg m}^{-3}$ ) and the lower part of the ISOW layer ( $\sigma_0 > 27.855 \text{ kg m}^{-3}$ ) forms a mixing line between ISOW at  $2.8^\circ\text{C}/34.94$  and DSOW at  $1.5^\circ\text{C}/34.9$ . The inflow  
255 of DSOW is possibly sourced by the recirculation evidenced by the two floats in the vicinity of Greenland. Hence, the northward erosion of the ISOW core reveals a compensation between cold and fresh inflow **from the Irminger Sea** and saltier and warmer BFZ through-flow, which maintains a maximum in salinity for the ISOW layer at these latitudes.

#### 4 Discussion and Conclusion

A combination of new and insightful data sets allows us to investigate the role of the BFZ as a new source of ISOW for the  
260 Irminger Current flowing northward from the CGFZ. We first document ISOW pathways within the BFZ and its hydrological evolution by analyzing data from hydrographic sections and three Deep-Arvor floats deployed at specific locations through the BFZ between 2015 and 2018. From east to west, the hydrographic sections were acquired at the Eastern Sill, within the rift valley and through **basins** west of the Western Sill. This combination of observational datasets reveals that the BFZ is mainly fed by the lighter part of the ISOW layer flowing west of  $29\text{-}30^\circ\text{W}$  near  $58^\circ\text{N}$ , as part of the East Reykjanes Ridge Current  
265 (ERRC) in the Iceland Basin. ISOW is then channelled in the BFZ by the narrow and deep bathymetry of its Eastern Sill with an averaged ISOW transport of  $0.6 \pm 0.2 \text{ Sv}$  in 2015 and 2017.

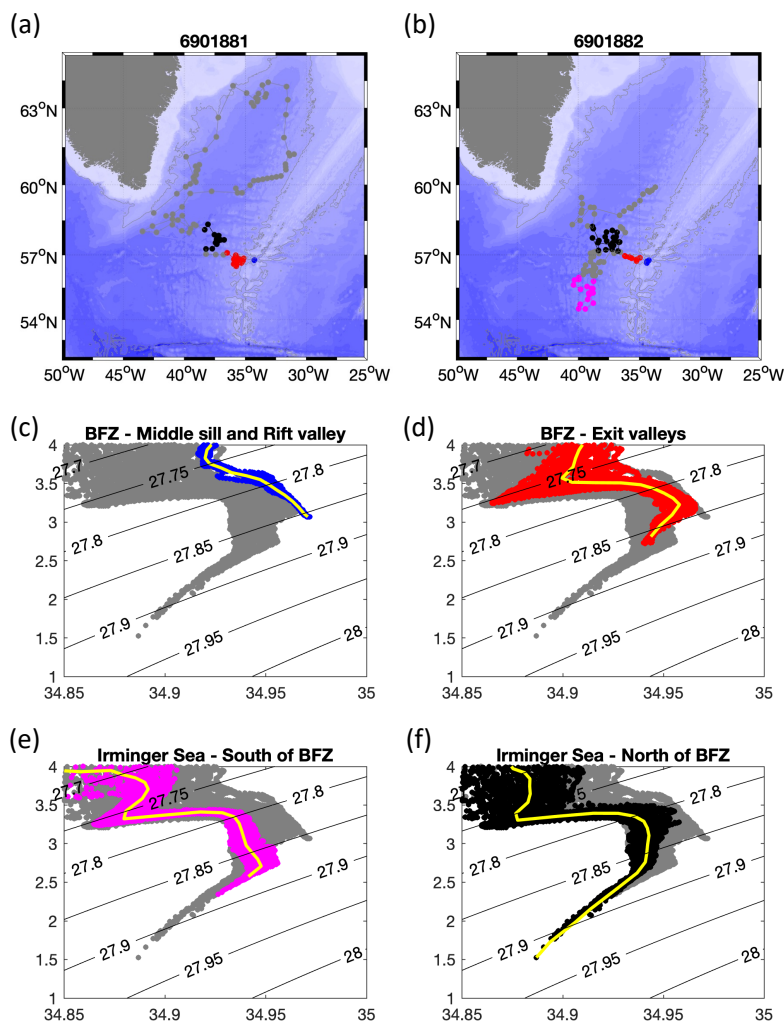


**Figure 6.** (a-b) Trajectories of Deep-Arvor floats #6902881 and #6902882 from the Middle section with dots locating profiles distant of 10-days. (c-f) Associated  $\theta$ -S profiles for the ISOW density range. Colors in  $\theta$ -S plots refer to the location of the profiles in panels (a-b), from the interior of the BFZ (blue dots) to the interior of the Irminger Sea north of the BFZ (black dots). In yellow are the averaged properties of the colored profiles.

Once in the rift valley, the circulation within the ISOW layer is cyclonic with an averaged transport of  $0.76 \pm 0.2$  Sv. The difference in ISOW transport between the East and the Middle sections in 2015 suggests that **additional deep inflows** ( $< 1$  Sv) could join the rift valley from shallower valleys north of the Eastern Sill. This is further confirmed by the ISOW transports of  $-0.3 \pm 0.1$  Sv in 2015 and  $-0.46 \pm 0.1$  Sv in 2016 estimated in a valley immediately north of the Eastern Sill (56.85-56.95°N) and sampled during RREX15 and BOCATS16 (Figure 1 b-c).

The cyclonic circulation of ISOW in the rift valley is associated with a strong homogenization of the ISOW layer, which highlights a vertical mixing within the layer, but not an intense **isopycnal mixing** with surrounding lighter water masses.



We note that the coldest core of ISOW is localized along the **left hand side** of the westward current (e.g. southern wall) in the  
280 rift valley, and is associated with an inversion of the isopycnal slopes below ~1500 m. Frey et al. (2019) found similar  
inversions through various fracture zones in the Atlantic and explained these structures by bottom friction. The bottom Ekman  
flux modifies the structure of the flow across the channel and displaces the coldest core of the overflow along the left-hand  
side of the current in the northern hemisphere.

Before joining the Irminger Sea, ISOW exits the BFZ along the northern walls of two western **basins** localized downstream of  
285 the Western Sill to the west of the rift valley. There, the BFZ through-flow encounters fresher and colder inflow from the  
Irminger Sea. The associated **isopycnal mixing** between these water masses induces a strong freshening of the BFZ through-  
flow in its upper layer. In its lower layer, ISOW is mainly composed of fresh and cold inflow from the Irminger Sea. The  
superposition of these two ISOW layers creates a maximum in salinity at  $27.83 \text{ kg m}^{-3}$ .

Previous papers highlight the role of bathymetry in the mixing of deep waters (De Lavergne et al., 2017). For instance, the  
290 equatorial densest water masses of the Romanche and Chain fracture zones were strongly modified by vertical mixing  
downstream of the sills (Ferron et al., 1998; Mercier et al., 1994; Mercier & Morin, 1997). Studies in the CGFZ also show the  
influence of North Atlantic Current into the mixing of ISOW with surrounding water masses (Bower & Furey, 2017; Racapé  
et al., 2019). At the BFZ, our analysis suggests that another mechanism is in place downstream of the Western Sill. Indeed,  
we observe a strong **isopycnal mixing** between ISOW of different origins within the western basins of the BFZ, but this mixing  
295 does not reach the bottom and does not seem to be driven by strong currents at surface.

The impact of the BFZ through-flow on the Irminger Current is then investigated by comparing the ISOW properties in the  
vicinity of the CGFZ and BFZ. We show that the core of ISOW observed at CGFZ is eroded toward lower densities as ISOW  
reaches BFZ latitudes, which possibly leads to the asymmetry of the ISOW properties observed along the so-call OVIDE  
section (Danialt et al., 2016; Petit et al., 2019). This erosion is driven by a combination of fresh inflows from the Irminger  
300 Sea and salty outflows from the BFZ. The inflow of dense water from the interior of the Irminger Sea has been estimated to  
**1.4 Sv by Petit et al. (2019). Hence, our analysis reveals the key role of the BFZ through-flow in the compensation of the  
ISOW freshening in the Irminger Sea. This result can provide benchmarks for the validation of ocean models at high resolution.**

The southward propagation of a Deep-Arvor float along the western flank of the Reykjanes Ridge is possibly explained by  
southward currents observed west of the Irminger Current at OVIDE latitudes (de Jong et al., 2020; Lherminier et al., 2007;  
305 Sarafanov et al., 2012; Våge et al., 2011) and at  $56.4^\circ\text{N}$  along the Reykjanes Ridge (Petit et al., 2019). Then, the propagation  
of this Deep-Arvor float suggests that these southward currents are not **local** artefact of measurements but are connected along  
the length of the Reykjanes Ridge.

The Deep-Arvor pathways can also provide insights about the spreading of ISOW in the Irminger Sea. Interestingly, the two  
floats sampled a similar circulation pattern at a few week interval: they headed northwestward to reach the tip of Greenland,  
310 and then **gets** abruptly diverted northeastward into the Irminger Current. This propagation pathway in the Irminger Sea reveals



that the BFZ through-flow follows interior pathways before joining the Irminger Current further north. This propagation pathway agrees with previous papers showing that the Irminger Current continuously includes inflows from the western subpolar gyre (Lavender et al., 2005; Petit et al., 2019). Similarly, Racapé et al. (2019) showed that one of the Deep-Arvor float launched at the CGFZ did not follow the well-known ISOW cyclonic circulation in the Irminger Sea. Instead, the float headed southwestward and directly reached the western boundary current near Newfoundland. Also, an abrupt diversion close to the shelfbreak of Cape Farewell is consistent with recirculation of the East Greenland Current and Deep Western Boundary Current into the interior of the Irminger Sea at the Eirik Ridge (Holliday et al., 2007; Pacini et al., 2020).

Finally, the temporal evolution of the ISOW properties that enter the BFZ can be assessed by comparing the East and Middle sections between the four cruises (Figures 3, A1 and A2). Overall, the ISOW temperature does not show large changes from 2015 to 2018 at these two locations, while the ISOW salinity decreased by about 0.01 between 2015 and 2018. The decrease in salinity at the BFZ entrance is close to that observed at the OVIDE section. An investigation of this freshening is beyond the scope of our study, but we note that an ISOW freshening is consistent with the overall freshening of the Iceland Basin in the upper layer of the MOC (Holliday et al., 2020), as the upper ocean salinity anomaly propagates in the ISOW layer by entrainment along the Icelandic shelf (Devana et al., 2021).

325

*Data availability.* The hydrographic data obtained during the four cruises are archived online at <https://www.seanoe.org/data/00443/55445/> for RREX15 and RREX17, at <https://digital.csic.es/handle/10261/154341> for BOCATS16 and at <https://www.seanoe.org/data/00762/87394/> for OVIDE18. The Deep-Arvor data of the floats used in this study are available at the Argo float data and metadata from Global Data Assembly Centre (Argo GDAC), <https://doi.org/10.17882/42182>. These data were collected and made freely available by the International Argo Program and the national programs that contribute to it (<https://argo.ucsd.edu>, <https://www.ocean-ops.org>). The Argo Program is part of the Global Ocean Observing System.

*Author contributions.* T.P., V.T. and H.M. led the analysis and interpretation of the data. All the authors contributed to writing of the manuscript.

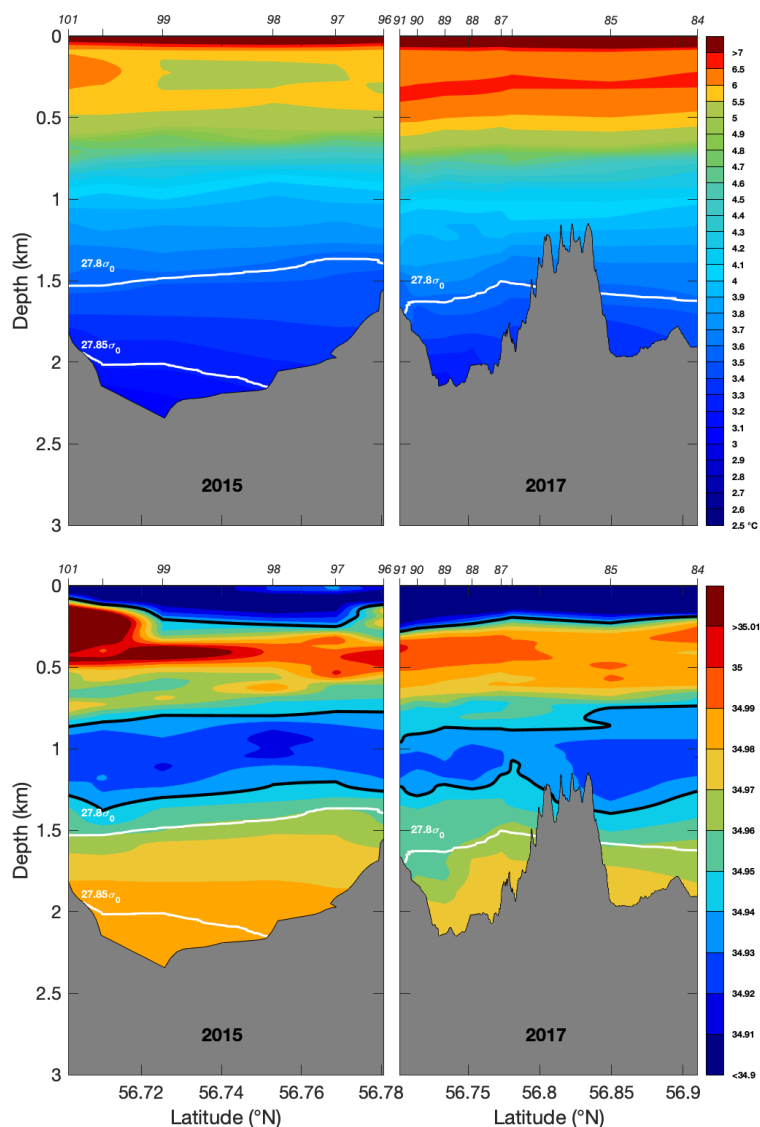
*Competing interests.* The authors declare no competing interests.

#### *Acknowledgements.*

This work was carried out within the framework of the NAOS and ARGO-2030 projects. The two projects received the support of the French government within the framework of the "Investissements d'avenir" program managed by the Agence Nationale de la Recherche (ANR) under the references ANR-10-EQPX-40 and ANR-21-ESRE-0019. The authors thank all colleagues and ship crews involved in the RREX and OVIDE cruises during which the hydrography data were obtained. The OVIDE project was supported by CNRS, Ifremer, the national program LEFE (Les Enveloppes Fluides et l'Environnement) and the Spanish Ministry of Sciences and Innovation co-funded by the BOCATS2 Project (PID2019-104279GB-C21) and ARIOS project (CTM2016-76146-C3-1-R).

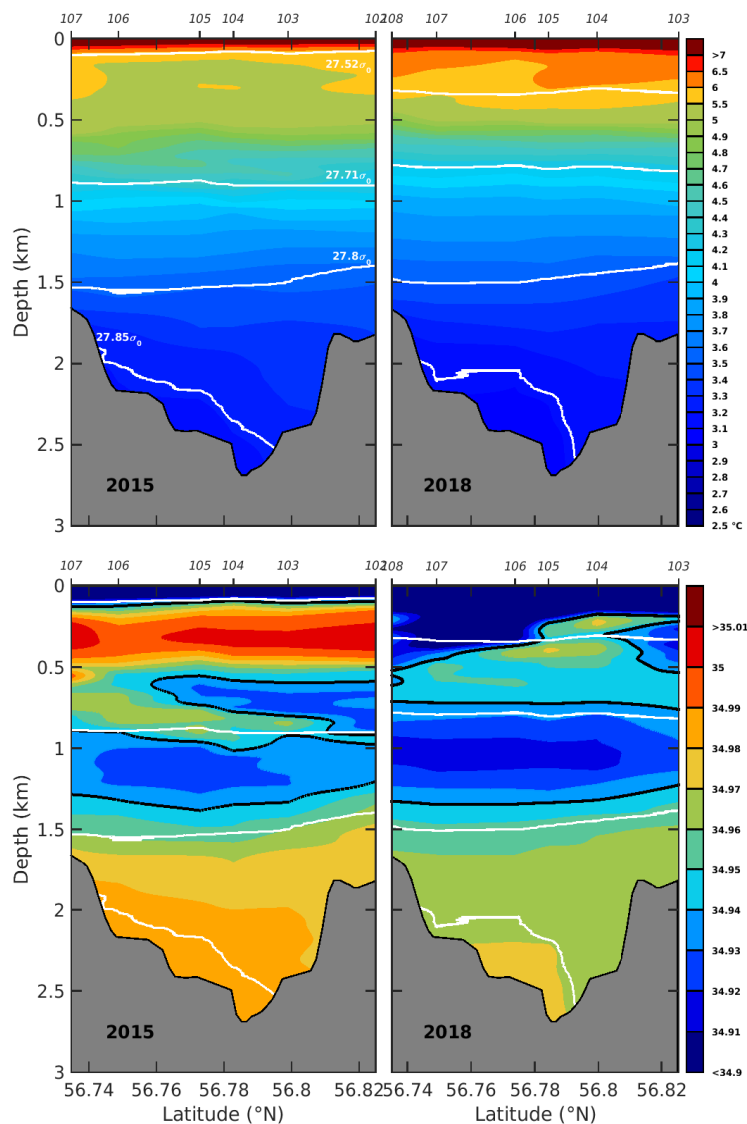


## Appendix A

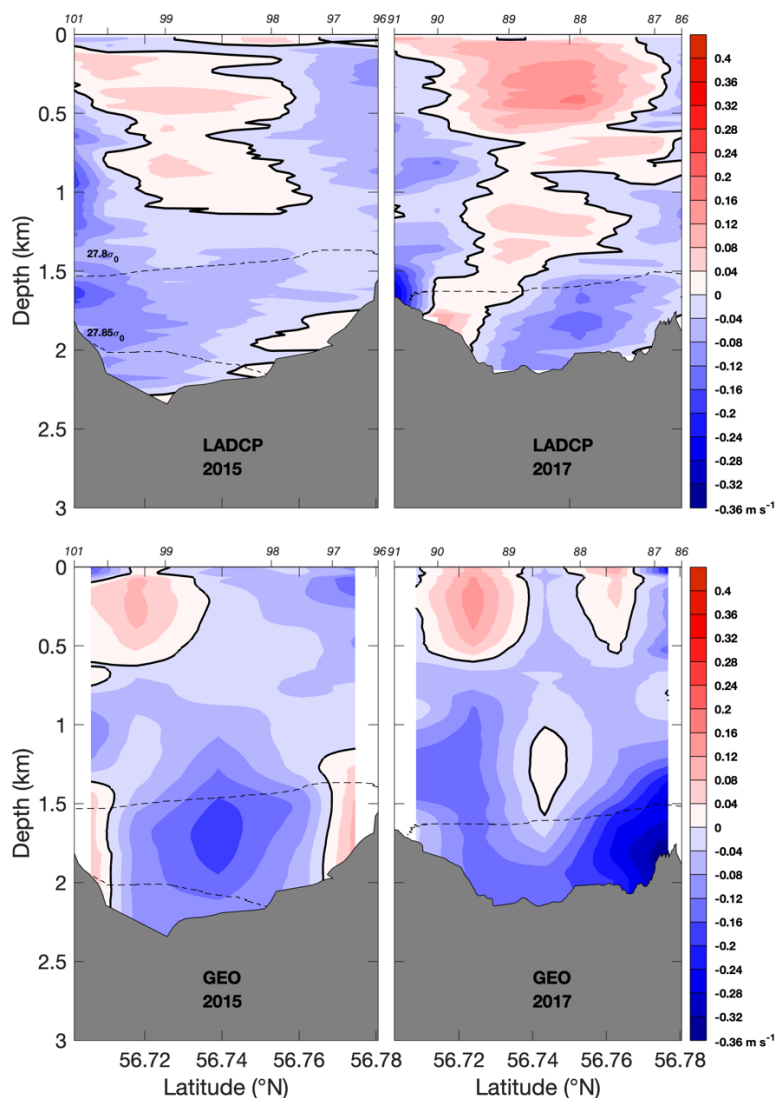


350 **Figure A1.** Hydrographic sections along the East sections 2015 and 2017 based on CTDO2 data for (upper panels) potential temperature in °C and (lower panels) salinity. The bold black lines represent isohaline 34.94 for the lower panels. In all panels, the bold white lines show the potential density anomalies  $\sigma_0 = 27.52, 27.71, 27.8$  and  $27.85 \text{ kg m}^{-3}$ . Bathymetries in grey are from the ship surveys. Locations and numbers of the hydrographic stations are indicated on the top axis.



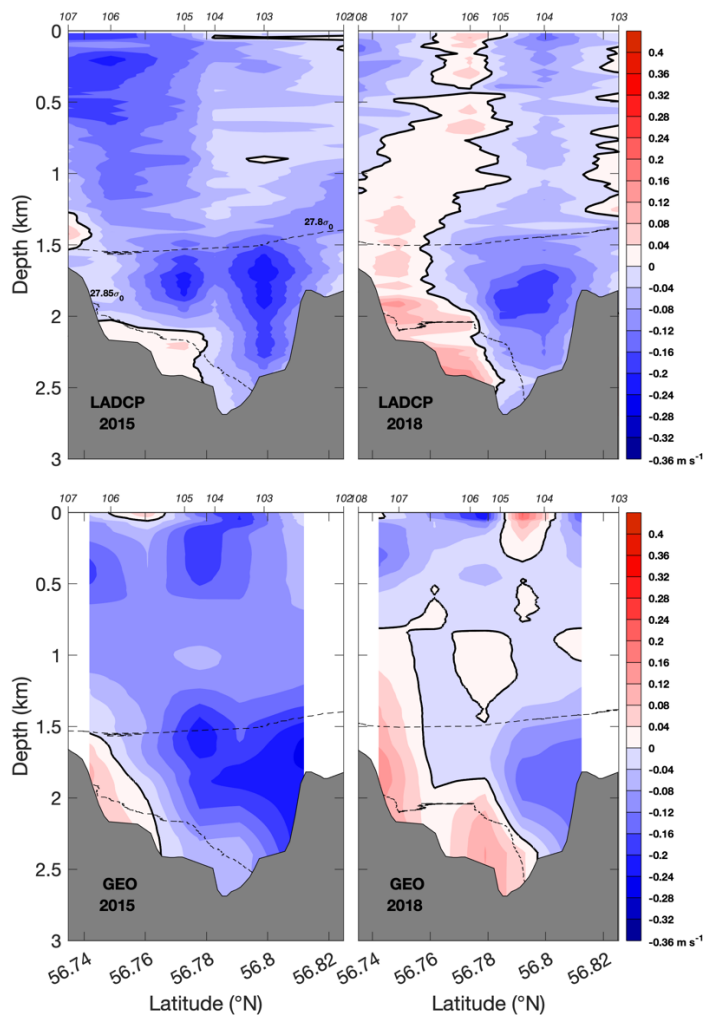


355 **Figure A2.** Hydrographic sections along the Middle sections 2015 and 2018 based on CTDO2 data for (upper panels) potential temperature in °C and (lower panels) salinity. The bold black lines represent isohaline 34.94 for the lower panels. In all panels, the bold white lines show the potential density anomalies  $\sigma_0 = 27.52, 27.71, 27.8$  and  $27.85 \text{ kg m}^{-3}$ . Bathymetry in grey is from the ship surveys. Locations of the hydrographic stations are indicated on the top axis.



360

**Figure A3.** (upper panels) L-ADCP and (lower panels) Geostrophic velocity sections along the East sections 2015 and 2017 ( $\text{m s}^{-1}$ ). Positive values correspond to eastward velocities. The black bold line outlines the 0 isotach. The dashed black lines indicate the potential density  $\sigma_0 = 27.52, 27.71, 27.8$  and  $27.85 \text{ kg m}^{-3}$ . Bathymetries from the ship surveys are added in grey. Locations of the hydrographic stations are indicated on the top axis.



365

**Figure A4.** (upper panels) L-ADCP and (lower panels) Geostrophic velocity sections along the Middle sections 2015 and 2018 ( $\text{m s}^{-1}$ ). Positive values correspond to eastward velocities. The black bold line outlines the 0 isotach. The dashed black lines indicate the potential density  $\sigma_0 = 27.52, 27.71, 27.8$  and  $27.85 \text{ kg m}^{-3}$ . Bathymetries from the ship surveys are added in grey. Locations of the hydrographic stations are indicated on the top axis.

370



## References

- 375 Bower, A., & Furey, H. (2017). Iceland-Scotland Overflow Water transport variability through the Charlie-Gibbs Fracture Zone and the impact of the North Atlantic Current. *Journal of Geophysical Research: Oceans*, 122(9), 6989–7012. <https://doi.org/10.1002/2017JC012698>
- Bower, A., Le Cann, B., Rossby, T., Zenk, W., Gould, J., Speer, K., Richardson, P. L., Prater, M. D., & Zhang, H. M. (2002). Directly measured mid-depth circulation in the northeastern North Atlantic Ocean. *Nature*, 419(6907), 603–607.  
380 <https://doi.org/10.1038/nature01078>
- Branellec, P., & Lherminier, P. (2017). BOCATS 2016. CTD-O2 data report. *Int. Rep. LOPS/17-06*. <https://doi.org/https://doi.org/10.13155/59190>
- Branellec, P., Lherminier, P., Reynaud, T., & Le Bihan, C. (2019). OVIDE 2018. CTD-O2 Data report. *ODE/LOPS/19-01*. <https://doi.org/https://doi.org/10.13155/86588>
- 385 Branellec, P., & Thierry, V. (2018). RREX 2017. CTD-O2 Data report. *Rap. Int. LOPS/18-04*. <https://doi.org/https://doi.org/10.13155/58074>
- Branellec, Pierre, & Thierry, V. (2016). RREX 2015. CTD-O2 Data report. *ODE/LOPS/16-26*. <https://doi.org/http://doi.org/10.13155/47156>
- Cabanes, C., Thierry, V., & Lagadec, C. (2016). Improvement of bias detection in Argo float conductivity sensors and its application in the North Atlantic. *Deep-Sea Research Part I: Oceanographic Research Papers*, 114, 128–136.  
390 <https://doi.org/10.1016/j.dsr.2016.05.007>
- Daniault, N., Mercier, H., Lherminier, P., Sarafanov, A., Falina, A., Zunino, P., Pérez, F. F., Ríos, A. F., Ferron, B., Huck, T., Thierry, V., & Gladyshev, S. (2016). The northern North Atlantic Ocean mean circulation in the early 21st century. *Progress in Oceanography*, 146(June), 142–158. <https://doi.org/10.1016/j.poccean.2016.06.007>
- 395 de Jong, M. F., de Steur, L., Fried, N., Bol, R., & Kritsotakis, S. (2020). Year-Round Measurements of the Irminger Current: Variability of a Two-Core Current System Observed in 2014–2016. *Journal of Geophysical Research: Oceans*, 125(10). <https://doi.org/10.1029/2020JC016193>
- De Lavergne, C., Madec, G., Roquet, F., Holmes, R. M., & McDougall, T. J. (2017). Abyssal ocean overturning shaped by seafloor distribution. *Nature*, 551(7679), 181–186. <https://doi.org/10.1038/nature24472>
- 400 Devana, M. S., Johns, W. E., Houk, A., & Zou, S. (2021). Rapid Freshening of Iceland Scotland Overflow Water Driven By Entrainment of a Major Upper Ocean Salinity Anomaly. *Geophysical Research Letters*, 1–11. <https://doi.org/10.1029/2021gl094396>
- Ferron, B., Kokoszka, F., Mercier, H., Lherminier, P., Huck, T., Rios, A., & Thierry, V. (2016). Variability of the Turbulent Kinetic Energy Dissipation along the A25 Greenland–Portugal Transect Repeated from 2002 to 2012. *Journal of Physical Oceanography*, 46(7), 1989–2003. <https://doi.org/10.1175/JPO-D-15-0186.1>  
405
- Ferron, B., Mercier, H., Speer, K., Gargett, A., & Polzin, K. (1998). Mixing in the Romanche Fracture Zone. *Journal of Physical Oceanography*, 28(10), 1929–1945. [https://doi.org/10.1175/1520-0485\(1998\)028<1929:MITRFZ>2.0.CO;2](https://doi.org/10.1175/1520-0485(1998)028<1929:MITRFZ>2.0.CO;2)



- 410 Frey, D. I., Morozov, E. G., Fomin, V. V., Diansky, N. A., & Tarakanov, R. Y. (2019). Regional Modeling of Antarctic Bottom Water Flows in the Key Passages of the Atlantic. *Journal of Geophysical Research: Oceans*, *124*(11), 8414–8428. <https://doi.org/10.1029/2019JC015315>
- Hansen, B., & Østerhus, S. (2000). North Atlantic–Nordic Seas exchanges. *Progress in Oceanography*, *45*(2), 109–208. [https://doi.org/10.1016/S0079-6611\(99\)00052-X](https://doi.org/10.1016/S0079-6611(99)00052-X)
- 415 Holliday, N. P., Bersch, M., Berx, B., Chafik, L., Cunningham, S., Florindo-López, C., Hátún, H., Johns, W., Josey, S. A., Larsen, K. M. H., Mulet, S., Oltmanns, M., Reverdin, G., Rossby, T., Thierry, V., Valdimarsson, H., & Yashayaev, I. (2020). Ocean circulation causes the largest freshening event for 120 years in eastern subpolar North Atlantic. *Nature Communications*, *11*(1), 585. <https://doi.org/10.1038/s41467-020-14474-y>
- Holliday, N. P., Meyer, A., Bacon, S., Alderson, S. G., & de Cuevas, B. (2007). Retroflexion of part of the east Greenland current at Cape Farewell. *Geophysical Research Letters*, *34*(7), 1–5. <https://doi.org/10.1029/2006GL029085>
- 420 Johns, W. E., Devana, M., Houk, A., & Zou, S. (2021). Moored Observations of the Iceland-Scotland Overflow Plume Along the Eastern Flank of the Reykjanes Ridge. *Journal of Geophysical Research: Oceans*, *126*(8), 1–26. <https://doi.org/10.1029/2021JC017524>
- Kanzow, T., & Zenk, W. (2014). Structure and transport of the Iceland Scotland Overflow plume along the Reykjanes Ridge in the Iceland Basin. *Deep-Sea Research Part I: Oceanographic Research Papers*, *86*, 82–93. <https://doi.org/10.1016/j.dsr.2013.11.003>
- 425 Koman, G., Johns, W. E., & Houk, A. (2020). Transport and Evolution of the East Reykjanes Ridge Current. *Journal of Geophysical Research: Oceans*, *125*(10). <https://doi.org/10.1029/2020JC016377>
- Lavender, K. L., Brechner Owens, W., & Davis, R. E. (2005). The mid-depth circulation of the subpolar North Atlantic Ocean as measured by subsurface floats. *Deep-Sea Research Part I: Oceanographic Research Papers*, *52*(5), 767–785. <https://doi.org/10.1016/j.dsr.2004.12.007>
- 430 Le Reste, S., Dutreuil, V., André, X., Thierry, V., Renault, C., Le Traon, P. Y., & Maze, G. (2016). “Deep-Arvor”: A new profiling float to extend the argo observations down to 4000-m depth. *Journal of Atmospheric and Oceanic Technology*, *33*(5), 1039–1055. <https://doi.org/10.1175/JTECH-D-15-0214.1>
- Le Traon, P.-Y., D’Ortenzio, F., Babin, M., Leymarie, E., Marec, C., Pouliquen, S., Thierry, V., Cabanes, C., Claustre, H., Desbruyères, D., Lacour, L., Lagunas, J.-L., Maze, G., Mercier, H., Penkerç’h, C., Poffa, N., Poteau, A., Prieur, L., Racapé, V., ... Xing, X. (2020). Preparing the New Phase of Argo: Scientific Achievements of the NAOS Project. *Frontiers in Marine Science*, *7*. <https://doi.org/10.3389/fmars.2020.577408>
- 435 Lherminier, P., Mercier, H., Gourcuff, C., Alvarez, M., Bacon, S., & Kermabon, C. (2007). Transports across the 2002 Greenland-Portugal Ovide section and comparison with 1997. *Journal of Geophysical Research: Oceans*, *112*(7), C07003. <https://doi.org/10.1029/2006JC003716>
- 440 Lozier, M. S., Bower, A. S., Furey, H. H., Drouin, K. L., Xu, X., & Zou, S. (2022). Overflow Water Pathways in the North Atlantic. *Progress in Oceanography*, under revision
- Mercier, H., & Morin, P. (1997). Hydrography of the Romanche and Chain Fracture Zones. *Journal of Geophysical Research: Oceans*, *102*(C5), 10373–10389. <https://doi.org/10.1029/97JC00229>
- 445 Mercier, H., Speer, K. G., & Honnorez, J. (1994). Flow pathways of bottom water through the Romanche and chain fracture zones. *Deep-Sea Research Part I*, *41*(10), 1457–1477. [https://doi.org/10.1016/0967-0637\(94\)90055-8](https://doi.org/10.1016/0967-0637(94)90055-8)



- 450 Pacini, A., Pickart, R. S., Bahr, F., Torres, D. J., Ramsey, A. L., Holte, J., Karstensen, J., Oltmanns, M., Straneo, F., Le Bras, I. A., Moore, G. W. K., & Femke de Jong, M. (2020). Mean conditions and seasonality of the west Greenland boundary current system near cape farewell. *Journal of Physical Oceanography*, 50(10), 2849–2871. <https://doi.org/10.1175/JPO-D-20-0086.1>
- Petit, T., Mercier, H., & Thierry, V. (2019). New Insight Into the Formation and Evolution of the East Reykjanes Ridge Current and Irminger Current. *Journal of Geophysical Research: Oceans*, 124(12), 9171–9189. <https://doi.org/10.1029/2019JC015546>
- 455 Petit, T., Mercier, H., & Thierry, V. (2018). First direct estimates of volume and water mass transports across the Reykjanes Ridge. *Journal of Geophysical Research: Oceans*. <https://doi.org/10.1029/2018JC013999>
- Racapé, V., Thierry, V., Mercier, H., & Cabanes, C. (2019). ISOW Spreading and Mixing as Revealed by Deep-Argo Floats Launched in the Charlie-Gibbs Fracture Zone. *Journal of Geophysical Research: Oceans*, 124(10), 6787–6808. <https://doi.org/10.1029/2019JC015040>
- 460 Sarafanov, A., Falina, A., Mercier, H., Sokov, A., Lherminier, P., Gourcuff, C., Gladyshev, S., Gaillard, F., & Daniault, N. (2012). Mean full-depth summer circulation and transports at the northern periphery of the Atlantic Ocean in the 2000s. *Journal of Geophysical Research: Oceans*, 117(1), C01014. <https://doi.org/10.1029/2011JC007572>
- Saunders, P. M. (1994). The flux of overflow water through the Charlie-Gibbs Fracture Zone. *Journal of Geophysical Research*, 99(C6), 12343. <https://doi.org/10.1029/94JC00527>
- 465 Våge, K., Pickart, R. S., Sarafanov, A., Knutsen, Ø., Mercier, H., Lherminier, P., van Aken, H. M., Meincke, J., Quadfasel, D., & Bacon, S. (2011). The Irminger Gyre: Circulation, convection, and interannual variability. *Deep-Sea Research Part I: Oceanographic Research Papers*, 58(5), 590–614. <https://doi.org/10.1016/j.dsr.2011.03.001>
- Wong, A., Keeley, R., Carval, T., & the Argo Data Management Team. (2021). *Argo Quality Control Manual for CTD and Trajectory Data*. <https://doi.org/http://dx.doi.org/10.13155/33951>
- 470 Xu, X., Schmitz, W. J., Hurlburt, H. E., Hogan, P. J., & Chassignet, E. P. (2010). Transport of Nordic Seas overflow water into and within the Irminger Sea: An eddy-resolving simulation and observations. *Journal of Geophysical Research: Oceans*, 115(12), C12048. <https://doi.org/10.1029/2010JC006351>
- Zou, S., Bower, A., Furey, H., Susan Lozier, M., & Xu, X. (2020). Redrawing the Iceland–Scotland Overflow Water pathways in the North Atlantic. *Nature Communications*, 11(1). <https://doi.org/10.1038/s41467-020-15513-4>
- 475 Zou, S., Lozier, S., Zenk, W., Bower, A., & Johns, W. (2017). Observed and modeled pathways of the Iceland Scotland Overflow Water in the eastern North Atlantic. *Progress in Oceanography*, 159(September), 211–222. <https://doi.org/10.1016/j.pocean.2017.10.003>